
Beyond Geometry: Comparing the Temporal Structure of Computation in Neural Circuits with Dynamical Similarity Analysis

Mitchell Ostrow, Adam Eisen, Leo Kozachkov, Ila Fiete

Department of Brain and Cognitive Sciences, MIT

Cambridge, MA, USA

{ostrow, eisenaj, leokoz8, fiete}@mit.edu

Abstract

How can we tell whether two neural networks are utilizing the same internal processes for a particular computation? This question is pertinent for multiple sub-fields of both neuroscience and machine learning, including neuroAI, mechanistic interpretability, and brain-machine interfaces. Standard approaches for comparing neural networks focus on the spatial geometry of latent states. Yet in recurrent networks, computations are implemented at the level of neural dynamics, which do not have a simple one-to-one mapping with geometry. To bridge this gap, we introduce a novel similarity metric that compares two systems at the level of their dynamics. Our method incorporates two components: Using recent advances in data-driven dynamical systems theory, we learn a high-dimensional linear system that accurately captures core features of the original nonlinear dynamics. Next, we compare these linear approximations via a novel extension of Procrustes Analysis that accounts for how vector fields change under orthogonal transformation. Via four case studies, we demonstrate that our method effectively identifies and distinguishes dynamic structure in recurrent neural networks (RNNs), whereas geometric methods fall short. We additionally show that our method can distinguish learning rules in an unsupervised manner. Our method therefore opens the door to novel data-driven analyses of the temporal structure of neural computation, and to more rigorous testing of RNNs as models of the brain.

1 Introduction

Comparing neural responses between different systems or contexts plays many crucial roles in neuroscience. These include comparing a model to experimental data (as a measure of model quality, Schrimpf et al. [2020]), determining invariant states of a neural circuit (Chaudhuri et al. [2019]), identifying whether two individual brains are performing a computation in the same way, aligning recordings across days for a brain-machine interface (Degenhart et al. [2020]), and comparing two models (e.g. to probe the similarity of two solutions to a problem, Pagan et al. [2022]). Current similarity methods include R^2 via Linear Regression, Representational Similarity Analysis, Singular Vector Canonical Correlation Analysis, Centered Kernel Alignment, and Procrustes Analysis (Schrimpf et al. [2020], Kriegeskorte et al. [2008], Raghu et al. [2017], Williams et al. [2021], Duong et al. [2022]). Crucially, these all compare the *geometry* of states in the latent space of a neural network. The importance of identifying shared neural computations between systems calls for comparison methods that capture similarity at the relevant levels of abstraction.

In the brain and in RNNs, a popular model of biological neural networks, computations are instantiated by the emergent dynamical properties of the network, such as fixed points, invariant and fixed point

manifolds, limit cycles, and transitions between them (Hopfield [1984], Hopfield and Tank [1986], Zhang [1996], Mongillo et al. [2008], Burak and Fiete [2009], Churchland et al. [2008], Sussillo and Abbott [2009], Churchland et al. [2012], Khona and Fiete [2022], Vyas et al. [2020]). When applied to dynamical systems, geometric similarity metrics fall short in two manners. First, response geometries can differ due to sampling differences or other non-fundamental causes even though the dynamics are topologically equivalent. In such cases, measures of state space geometry do not fully capture the core similarities between two systems (Maheswaranathan et al. [2019]), a false negative situation. Conversely, systems may exhibit distinct dynamics over similar geometries in the state space (Galgali et al. [2023]). In this case, geometric measures may fail to distinguish two distinct systems, a false positive situation. Therefore, we suggest that dynamical systems theory should be a lens through which to compare neural systems.

Here, we develop a data-driven method called Dynamical Similarity Analysis (DSA), which combines work from two previously-unrelated fields of machine learning for dynamical systems and statistical shape analysis. In brief, DSA returns a similarity metric describing how two systems compare at the level of their dynamics. DSA utilizes a high-dimensional embedding to identify a linear vector field representation of a nonlinear system, which captures spatiotemporally coherent features of its dynamics. These features, referred to as Koopman Modes (Koopman [1931], Mezić [2005]) and identified via the Dynamic Mode Decomposition (DMD), describe a system’s core dynamic structure (Snyder and Song [2021], Brunton et al. [2021]). Subsequently, a statistical shape analysis metric is used to compare these vector fields, thereby assessing the similarity between the systems’ dynamics. This shape analysis can be viewed as comparing the dynamical structure of the systems: both the dynamic modes (the vector field’s eigenvectors) in each system and their temporal properties (its eigenvalues), such as whether the modes grow, shrink, or oscillate, are compared. Unlike most spatial shape analyses, which require averaging over multiple noisy trials in the same condition to arrive at one ‘representation’ of each condition-time point (but see Duong et al. [2022]), DSA factors noise into its estimate of neural dynamics. The importance of these noise perturbations in capturing dynamics has been highlighted in Galgali et al. [2023], as their evolution over time can uniquely identify dynamic structure. Thus, DSA takes advantage of all available information.

Our results demonstrate that DSA effectively identifies the dynamic structure of neural computations, whereas standard geometric methods fall short. DSA therefore has great relevance for neuroscience, where knowledge of the underlying dynamics can only be inferred through measurements. Consequently, DSA provides another method to validate how well a model fits to neurophysiology data, and opens the door to novel data-driven analyses of the temporal structure of neural computation. We expect our method to be interesting to computational neuroscientists due to its theoretical richness, valuable to deep learning researchers as another tool through which to interpret neural networks, and useful for experimental neuroscientists due to its simplicity of implementation and ease of interpretation.

Contributions We develop a general method, DSA, for comparing two dynamical systems at the level of their dynamics. To do so, we introduce a modified form of Procrustes Analysis that accounts for how vector fields change under orthogonal transformations. We apply our method on four test cases, each demonstrating novel capabilities in neural data analysis: **(a)** Our method can identify dynamical similarities underlying systems with different geometries, which shape metrics cannot. **(b)** Conversely, DSA can distinguish systems with different dynamics despite similar geometries, which shape metrics cannot. **(c)** We show that our method empirically identifies topological similarities and differences between dynamical systems, as demonstrated by invariance under geometric deformation and variance under topological transformation. **(d)** We demonstrate how to use DSA to disentangle different learning rules in neural networks without supervision, by comparing how representations change across training.

2 Methods

2.1 Theoretical Motivation: Dynamic Mode Decomposition (DMD) and Embeddings

A major goal in dynamical systems theory is to reduce complex nonlinear dynamics to linear systems that are easily interpretable. One classical method involves searching for fixed points and identifying their properties via local linearization (Lyapunov’s indirect method, Sussillo and Barak [2013]), but

this is not possible for experimental systems as full access and control are required. Other methods such as Switching Linear Dynamical Systems (Linderman et al. [2016]) are limited in capturing global structure.

In light of these concerns, a class of data-driven methods based on the DMD (Schmid [2010]) have recently emerged. These methods approximate the Koopman operator, which linearizes a nonlinear system by embedding it into an infinite-dimensional Hilbert space (Brunton et al. [2016a, 2017], Snyder and Song [2021], Dubois et al. [2020]). The DMD identifies a linear transition operator between local dynamics: $X(t + \Delta t) = AX(t)$, where X comprises a data matrix of observables (functions of the state of the dynamical system). When applied to a sufficiently rich X , the DMD can capture global dynamical structure. One challenge of the method is identifying a nonlinear measurement subspace, which must be closed under the operation of A (a Koopman invariant subspace, Brunton et al. [2016b]). Here, we utilize the Hankel Alternative View of Koopman (HAVOK) (Brunton et al. [2017]), which fits the DMD to a delay-embedding of the data (a Hankel Matrix), such that one column of $X = [-x(t) - x(t-\tau) - \dots - x(t-p\tau)]^T$. The delay-embedding approach eliminates the difficulty of learning a nonlinear transformation of the data, and provides improved estimation capabilities over partially-observed systems (Kamb et al. [2020]). The latter capability arises thanks to Takens’ delay embedding theorem, which states that a delay embedding is diffeomorphic to the original system—that is, a partially-observed system can be fully reconstructed using a sufficient number of delays (Takens [1981]).

2.2 Dynamical Similarity Analysis (DSA)

Now, we introduce the Dynamical Similarity Analysis, a general method that leverages advances in both Statistical Shape Analysis and Dynamic Mode Decomposition to compare two neural systems at the level of their dynamics. Simply put, we fit a DMD or its extensions to observations from two neural systems, and compare their dynamic mode matrices via a modified shape analysis metric.

Suppose we have two dynamical systems defined by the following equations:

$$\dot{\mathbf{x}} = f(\mathbf{x}, t) \quad \mathbf{x} \in \mathbb{R}^n \quad \dot{\mathbf{y}} = g(\mathbf{y}, t) \quad \mathbf{y} \in \mathbb{R}^m \quad (1)$$

We sample data from each system $X \in \mathbb{R}^{c \times k_1 \times t_1 \times n}$ and $Y \in \mathbb{R}^{c \times k_2 \times t_2 \times m}$. Here, c indicates the number of conditions observed, k indicates the number of trials per condition, and t indicates the number of time steps observed per trial. Note that the observations must be sampled uniformly in time (Takens [1981]). Next, we produce delay-embedded Hankel tensors with a lag of p : $H_x \in \mathbb{R}^{c \times k_1 \times (t-p-1) \times np}$ and likewise for H_y . Using the Hankel Alternative View of Koopman (HAVOK) approach (Brunton et al. [2017]), we flatten all but the last dimension of H and fit reduced-rank regression models with rank r to the eigen-time delay coordinates of the data, where the target is the coordinates of the next time step ($V'_{x,r}$):

$$V'_{x,r} = A_x V_{x,r} \text{ where } H_x = U_x \Sigma_x V_x^T \text{ and } V_{x,r} = V_x[:, 1 : r] \quad (2)$$

Only the rank of the HAVOK models explicitly need to be the same so that the two DMD matrices can be compared, but one could also be zero-padded such that the dimensions match (Williams et al. [2021]). We can assess the predictive capability of our model with MSE or R^2 . Hyperparameters of the DMD (lag p and rank r) for each experiment were chosen to ensure both sufficient capability to fit the dynamics in question as well as tractable computation times. Fitting the HAVOK model to each system returns our DMD matrices: $\mathbf{A}_x, \mathbf{A}_y \in \mathbb{R}^{r \times r}$, which we compare using the modified Procrustes Analysis algorithm detailed next.

Importantly, both the reduced-rank regression and delay-embedding are required to isolate dynamical structure. We demonstrate this in Fig. 1e, where we compare an RNN and GRU solving the Sine Wave task (Sussillo and Barak [2013]) using the standard Procrustes Analysis (via the netrep package, Williams et al. [2021]), delay-embedded Procrustes Analysis (an ablation), DSA with no delay embedding (another ablation), and DSA score. Only DSA identifies the systems as highly similar, indicating that both the delay embedding and the DMD are necessary to abstract geometric particulars from each system.

Procrustes Analysis over Vector Fields Procrustes Analysis is a valuable similarity metric, but to use it in DSA, we must modify the notion of orthogonal transformations to be compatible with vector

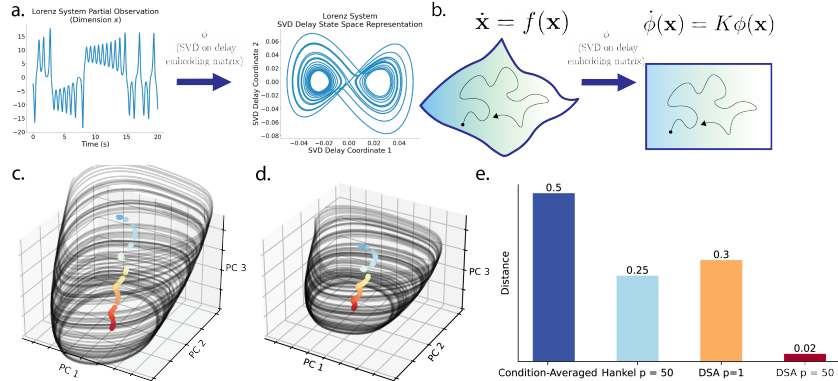


Figure 1: **Schematic and example of DSA.** **a.** Schematic of Delay Embedding. **b.** Schematic of the Koopman Operator computed on time-delay coordinates. **c,d.** PCA trajectories of a GRU (left) and Vanilla RNN trained to produce sine waves of a range of frequencies (Sussillo and Barak [2013]). Colored dots indicate center points of the limit cycles, colored by frequency of the output wave (black lines). **e.** Comparison of measured dissimilarity between the networks in **c,d** with (from left to right) Procrustes on the condition-averaged trajectories, Procrustes on the delay-embedded condition-averaged trajectories, DSA on the original data, and DSA on the delay embedding. Lower is more similar. Each metric uses angular distance, which ranges from 0 to π .

fields. Recall that the Procrustes metric solves the following minimization problem (Williams et al. [2021]):

$$d(\mathbf{X}, \mathbf{Y}) = \min_{\mathbf{C} \in O(n)} \|\mathbf{X} - \mathbf{C}\mathbf{Y}\|_F \quad (3)$$

Where $O(n)$ is the orthogonal group, F indicates the Frobenius norm, and X, Y are two data matrices. However, vector fields, represented by the DMD matrices $\mathbf{A}_x, \mathbf{A}_y$ above, transform differently than X and Y (see Supplementary Information for an illustration). The transformation $\mathbf{C}\mathbf{A}_y$ simply rotates vectors in place, which destroys dynamic structure (for example, it could turn a stable fixed point into an unstable one). However, $\mathbf{C}\mathbf{A}_y\mathbf{C}^{-1}$ rotates their positions as well, thereby preserving the vector field structure and satisfying the same goal as $\mathbf{C}\mathbf{Y}$ applied to a data matrix. Thus we introduce a novel similarity metric to the machine learning literature: Procrustes Analysis over Vector Fields:

$$d(\mathbf{A}_x, \mathbf{A}_y) = \min_{\mathbf{C} \in O(n)} \|\mathbf{A}_x - \mathbf{C}\mathbf{A}_y\mathbf{C}^{-1}\|_F \quad (4)$$

This nonconvex optimization problem is similar to Jimenez et al. [2013], although we solve it with gradient-based optimization. Across our experiments, we found that the metric asymptotes in less than 200 iterations using the Adam optimizer (Kingma and Ba [2014]) with a learning rate of 0.01. We derive this metric from first principles and prove that it is indeed a proper metric in the Supplementary Information, which as noted in Williams et al. [2021] is crucial for various downstream machine learning pipelines such as clustering or classification. In our experiments, we compare to Procrustes as it is the most similar shape metric to DSA. Note that other similarity metrics could also be modified to fit the DSA algorithm.

2.3 Model Architectures and Tasks

To demonstrate the viability of our method, we identified four illustrative cases that disentangle geometry and dynamics. First, a set of neural networks that shape analyses describe as different but dynamically are very similar; second, a set of neural networks that shape analyses describe as similar but dynamically are very different; third, a ring attractor network whose geometry we can smoothly deform while preserving the attractor topology; finally, a line attractor network that we transform into a ring attractor by transforming periodic boundary conditions.

Flip Flop For the first case, we train a collection of 50-unit RNNs on the well-known 3-bit Flip Flop task from Sussillo and Barak [2013] for the sake of space and its well-studied dynamical properties. Following Maheswaranathan et al. [2019], We varied architecture type (LSTM, GRU, UGRNN, Vanilla RNN), activation function (ReLU, Tanh), learning rate (.01,0.005), and multiple different seeds across each set of hyperparameters, ultimately collecting a dataset of 240 networks. We only saved a network if it solved the task with MSE less than 0.05. After training, we tested all models on the same 64 input sequences, and extracted the recurrent states, upon which we apply Procrustes and DSA in parallel to compare networks.

Perceptual Decision-Making To demonstrate the converse—same condition-averaged geometry with different topology—we examine a set of three noisy recurrent networks from Galgali et al. [2023]. These systems implement a bistable pair of attractors, a line attractor, and a single stable fixed point at the origin—their dynamical equations are included in the Supplementary Information. Here, the inputs to the latter two networks were adversarially optimized so that the condition-averaged trajectories are indistinguishable from the first network (Fig. 3a). These networks have intrinsic noise in their hidden states, which enables DSA to distinguish systems beyond condition-averages. We simulated 200 noisy trajectories from 100 networks per class, each with randomly sampled parameters.

Ring Attractor Deformations Next, we measure how DSA responds when geometric deformations are applied to a dynamical system, while preserving the topology. Here, we chose to study a ring attractor network, a system known to track head direction in the brain, and whose topology is a ring embedded in n neurons (Zhang [1996], Chaudhuri et al. [2019], Skaggs et al. [1995]). The neural activity on the ring is instantiated as a bump of local activity, which is stable due to local inhibition and global excitation. In each trial, we randomly sampled n uniformly between 100 and 250, and drove the network with constant input and dynamical noise, leading the bump to rotate around the ring at a constant velocity (we used code from Wang and Kang [2022]). The network’s dynamics are detailed in the Supplementary Information. Importantly, after each simulation, the activations can be transformed by a continuous deformation that preserves the ring topology while changing the geometry:

$$r = \frac{1}{1 + \exp(-\beta s)} \quad (5)$$

The variable s describes the synaptic activations of the ring network (the dynamical variable), and r describes the neural activations, which we compare with DSA and Procrustes. Here, β controls the width of the bump—at small β , the ring is essentially planar, and at large β , the ring is bent along each axis (see Fig. 1 in Kriegeskorte and Wei [2021] for a depiction). We scaled the magnitude of β from 0.1 to 4. After applying these transformations to simulated trajectories from our network, we applied DSA and Procrustes to respectively compare all β s to the lowest β in our dataset.

Transforming a Line into a Ring Finally, we assessed the converse to the previous analysis: does DSA respond to changes in topology? Using the same ring attractor, we varied the strength of its periodic boundary conditions to convert the ring into a curved line segment attractor by ablating some neurons from the network on one end of the ring. Our ring is defined by a cosine kernel that defines how each neuron connects to its neighbors. This kernel has a length parameter l which defines how far apart two neurons can connect. To completely eliminate the boundary conditions, l neurons must therefore be ablated. Using an ablation length c , we defined the following parameter:

$$\alpha = 1 - \frac{c}{l} \quad (6)$$

When $\alpha = 1$, the network is perfectly a ring, and breaks into a line segment when $\alpha < 1$. As $\alpha \rightarrow 0$ the ring becomes progressively less curved. To ensure that network sizes were consistent across all values of α , we initialized the network size to be $n + c$ before ablation, where n is the desired final number of neurons. We simulated networks of between 200 and 300 neurons. Instead of a constant drive of input as before, we drove the network with a fixed magnitude input u whose sign flipped stochastically. We chose this input to prevent the bump of activity from getting trapped on one side in the line attractor setting.

2.4 Learning Rule Disentangling with DSA

We applied DSA to two datasets containing neural networks trained with different learning rules: a dataset of observables from Nayebi et al. [2020] recorded from the hidden layers of large convolutional neural networks trained to solve three different tasks, and a set of small 3-layer neural networks (with a hidden size of 100 units) trained to solve a multivariate regression task from Bordelon and Pehlevan [2022]. The learning rules utilized in the first set include Adam (Kingma and Ba [2014]), Stochastic Gradient Descent with Momentum (Sutskever et al. [2013]), Information Alignment (Kunin et al. [2020]), and Feedback Alignment (Lillicrap et al. [2016]). The learning rules in the second set include Gradient Descent, two forms of Feedback Alignment that vary based on the initialization of the random feedback weights (Boopathy and Fiete [2022]), and Hebbian learning (Hebb [1949]). We apply DSA to trajectories of the neural representations (or observables) across training, such that our delay embeddings are computed over epochs. For each test set, we generate 200 sets of models total: In the first set, we generate 50 DMD matrices for each learning rule by randomly selecting trajectories from networks with the same learning rule to form a single dataset, and subsequently fitting a HAVOK model. In the second task, we generate 50 DMD matrices for each learning rule by fitting a single HAVOK model to 1000 epochs of training for a single model with a different random seed. We compare each model pairwise, which results in a representational dissimilarity matrix.

3 Results

3.1 DSA captures dynamical similarity between RNNs despite differences in geometry.

Our set of RNNs trained on the 3-bit Flip-Flop Task (Sussillo and Barak [2013]) have different representational geometry but equivalent attractor topology (Maheswaranathan et al. [2019]). Fig. 2 a. displays the trajectories of individual trials in a sample network in the first 3 Principal Components, which capture on average 95.9% of the total variance. The computational solution to this task is characterized by eight stable fixed points at the vertices of a cube that correspond to the eight possible unique memory states (2^3). Importantly, this cubic structure is preserved across all networks, even though particular geometric aspects of the trajectories may differ. Standard shape analyses differentiate architectures and activation function by geometry, which we replicated in Fig. 2 b (architecture) and in the Supplementary Information (activation).

We fit individual HAVOK models with 75 delays and rank 100 to sampled trajectories from each network. For computational efficiency, we reduced the dimensionality of the network to 10 using Principal Components Analysis (PCA) before applying HAVOK. By linearity of PCA, the dynamics of the original system within the PC subspace are preserved. For each pair of networks, we compared these states directly using Procrustes Analysis and on the DMD matrices using Procrustes Analysis on Vector Fields. This yields two Dissimilarity Matrices, which we reduced to two dimensions using Multidimensional Scaling (Kruskal [1964]). We plot the results in this similarity space in Fig. 2, where each point is a trained network. As expected, the networks cluster by architecture (Fig. 2b) and activation function (Supplementary Figures) when Procrustes is applied, indicating that aspects of their geometry differ. However, the networks intermingle under the DSA (Fig. 2c, inset zoomed in), and have pairwise dissimilarities close to zero, indicating that their underlying dynamics are equivalent, which is correct (Maheswaranathan et al. [2019]). We quantified these differences by applying a linear SVM to the dissimilarity matrices and plotted the test accuracy in Fig. 2d. This further underscores the differences between Procrustes and DSA in Fig. 2b and c, as DSA’s accuracy is close to chance, whereas Procrustes achieves high accuracy on both labels.

3.2 DSA identifies dynamical differences despite geometric similarity

Next, we sought to display the converse, namely that our similarity method can identify differences in dynamical structure even when spatial analysis cannot. We tested three models from Galgali et al. [2023], which implement different strategies for a classical perceptual decision-making task used in systems neuroscience: unstable evidence integration, stable integration, and leaky integration. We visualized the condition-averaged and single-trial trajectories in Fig. 3a for each dynamical system to confirm that the condition-averaged trajectories are indistinguishable.

We fit a HAVOK model with 100 lags and a rank of 50 for each network. As in Fig. 2, we computed both the spatial and dynamic dissimilarity matrices between each network and plotted them with

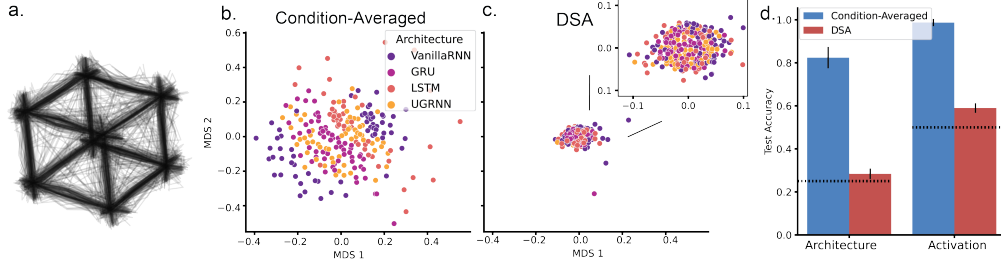


Figure 2: **Same dynamics, different shape, only identified as similar with DSA.** Dots indicate a single trained network. Analysis of RNNs trained on the 3-bit flipflop task. **a.** PCA trajectories of a single trained RNN. **b.** MDS Projection of the Dissimilarity Matrix computed across condition-averaged hidden states between each RNN (architecture indicated by color). In this view of the data, RNNs cluster by architecture. **c.** MDS Embedding of the dissimilarity matrix generated from DSA of the same set of RNNs as in b. Here, RNNs do not cluster by architecture. **d.** Classification test accuracy of condition-averaged Procrustes and DSA similarity spaces on both architecture and activation labels. Dotted lines indicate chance.

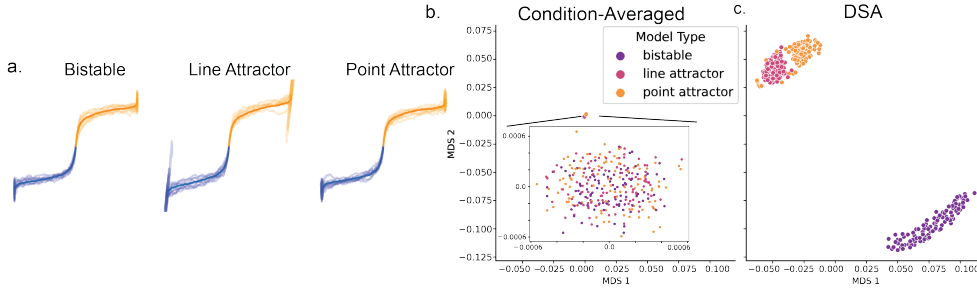


Figure 3: **Different dynamics, same shape, only distinguished by DSA.** **a.** Sample single-trial (faded) and condition-averaged trajectories of the three systems in two dimensions (x and y axes). Trials start at the center point and move away in a direction depending on the condition (colored). **b.** Shape analysis MDS on the RDMs of the three network types. **c.** DSA-MDS of the three networks.

MDS. Comparing the two types of similarities side by side (spatial similarity, Fig. 3b, and DSA, Fig. 3c), it is evident that only our method is able to easily distinguish dynamic types from the data alone. Thus, DSA can efficiently extract features that describe the underlying dynamical system from data alone, which better reflect the nature of the computation that is being performed in RNNs.

3.3 DSA is invariant under geometric deformations that preserve attractor topology

Here, we demonstrate that DSA compares two dynamical systems at the level of their topology. To do so, we smoothly deformed a ring attractor network in two manners and compared the original network to the progressively deformed system. Importantly, the simulated synaptic data is still the same in each case, so only the network’s geometry is deformed. In Fig. 4a we plot the first two PCs as the ring is progressively transformed with β (Fig. 4a). As we increase β , the width of the bump (see Supplementary Information for a visualization) becomes progressively tighter, which makes the ring less planar. This can also be measured by calculating the cumulative explained variance ratio of the first two PC’s, which starts at 99% at small β but drops to 30% at large β (Supplementary Information). We fit HAVOK models with a lag of 10 and a rank of 1000 to trajectories at each level of deformation. When we compared the network using DSA and Procrustes, we found that only DSA is invariant across these transformations (Fig. 4b,d). The value for DSA is not strictly zero, which may be due to approximation or numerical error in HAVOK and the similarity metric. Yet the dissimilarity measured by DSA is quite stable, with a standard deviation of 0.0175 across all trials **and** all β values. On the other hand, Procrustes had a standard deviation of 0.13 across trials

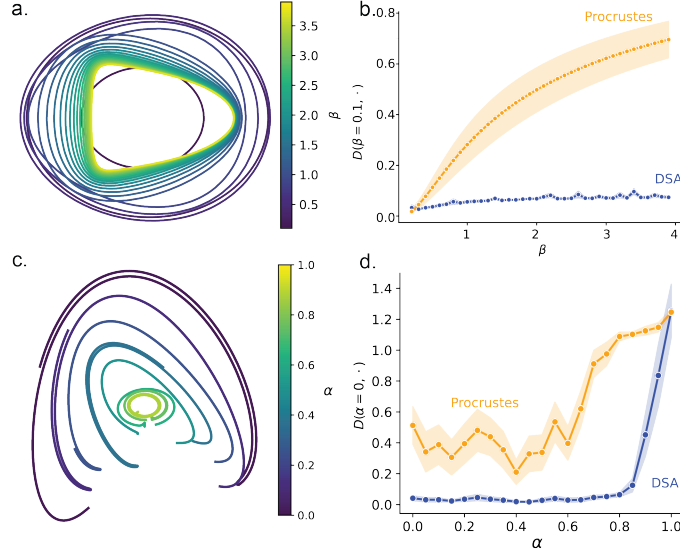


Figure 4: **DSA is invariant under geometric deformation of a ring attractor, and sensitive to the transformation of a ring attractor into a line.** Top row displays scaling of β in the sigmoid, making the ring progressively less planar. The bottom row displays topological transformation of a ring into a line via α . The network is a curve line attractor at $\alpha < 1$, and is a ring attractor at $\alpha = 1$. **a, c.** Trajectories along the ring plotted in the top two PCs of the network, colored by magnitude of the deformation parameter. In **c**, trajectories are scaled for visualization purposes. **b, d.** Distance (D) to $\beta = 0.1$, and $\alpha = 0.0$ in both Procrustes and DSA. Importantly, the topology only changes in the last row, at $\alpha = 1.0$.

per deformation value. This suggests that DSA identifies similarity at the level of the topology of a dynamical system.

3.4 DSA responds to changes in topology

We tested DSA on simulations of the ring network again as we smoothly varied the boundary conditions, thereby transforming the ring attractor into a line as α become progressively smaller. When we compared each value of α of the network to $\alpha = 0$ with DSA and Procrustes, we identified that DSA reports values close to 0 until α becomes close to 1.0, when it jumps almost to $\pi/2$. We plotted these results in Fig. 4, where panel **e** depicts the low-dimensional visualization of the line and the ring, and **f** displays our metric’s response. Note that because the method and data are stochastic, we expected DSA to jump slightly before 1.0, which we empirically verified to be around $\alpha = 0.9$ in our simulations. Here we used only 10 delays (for a total embedding size of 2500) and rank 100, but found that our results generalized to much larger DMD models as well. This further solidifies the notion that DSA captures topological similarity of two dynamical systems.

3.5 DSA can disentangle learning rules in an unsupervised fashion

It is still unclear what learning rules the brain uses. There has been significant progress recently, especially in the design of novel biologically-plausible learning rules (Lillicrap et al. [2016], Hinton [2022]), experiments and modeling work that suggests signs of gradient-based learning in the brain (Sadler et al. [2014], Humphreys et al. [2022], Payeur et al. [2023]), supervised methods to classify learning rules from aggregate statistics in neural data (Nayebi et al. [2020]), and theory describing how representations evolve across training in different learning rules (Bordelon and Pehlevan [2022]). Because artificial networks are initialized with random seeds, their trajectories in the activity space across learning will almost always have different geometry, despite the fact that they may converge to the same minimum. However, because the trajectories arise from the same dynamical system, DSA is invariant to random initializations. We visualize a variety of learning rule dynamics in Fig. 5a to demonstrate how qualitatively different these can be.

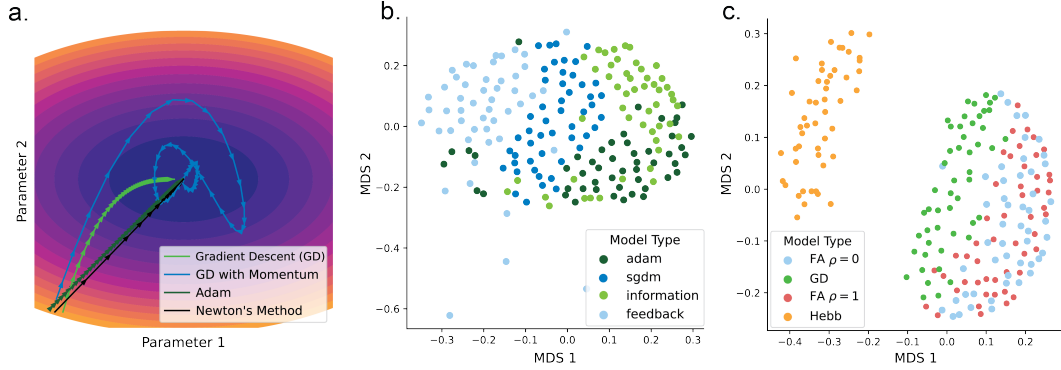


Figure 5: **DSA unsupervisedly disentangles learning rules.** **a.** Schematic example of different algorithms minimizing $3x^2 + 2y^2$. **b.** DSA MDS plot of hidden activation observables from networks trained on ImageNet **c.** DSA MDS plot of the dynamics of learning in 3-layer linear networks.

We applied DSA on two test cases from the literature to demonstrate that we can empirically disentangle artificial networks trained with different learning rules. In the first case, we use the dataset from Nayebi et al. [2020], which consists of aggregate statistics about the weights and activity of layers in various convolutional neural networks trained on various tasks and learning rules. We fit a HAVOK model with a rank of 45 and lag of 4 to trajectories of these statistics *across* training. After comparing trajectories of these observables across training with DSA, we visualize the MDS of the similarity space in Fig. 5b. The training dynamics clearly cluster by learning rule under DSA. Quantifying the degree of clustering, we could classify the learning rule with 88.5 % validation accuracy using only a *linear* classifier and 5-fold cross-validation, whereas the linear SVM classifier in Nayebi et al. [2020] only reached $\sim 55\%$ accuracy (Fig. 2a. in their paper). In the second case, a set of 3-layer feedforward linear networks from Bordelon and Pehlevan [2022], we fit HAVOK models to individual networks with a delay of 100 and a rank of 500. As above, we found that the MDS visualization of these networks clustered by learning rule in the pairwise similarity space (Fig. 5c). The two types of Feedback Alignment cluster together, suggesting that their dynamics are similar, as might be expected. Once again utilizing a linear classifier, we achieved 89% validation accuracy after assigning both types of FA as the same class. These results suggest the DSA could be used in a hypothesis-driven fashion to assess learning rules in data recorded from biological circuits.

4 Discussion

We demonstrated that our novel metric can be used to study dynamics in neural networks across numerous scenarios, including the comparison of dynamics across different RNNs, dynamics of a single RNN across training, or dynamics of weight and activity changes in feedforward networks across training. We performed an ablation study in Fig. 1e, which demonstrates that both delay embedding and the DMD were required for DSA to succeed. While we applied our metric only to RNNs, we stress that it can be applied to any dynamical system, including diffusion models or generative transformers. Procrustes Analysis over Vector Fields could also be applied to Koopman Embeddings identified via other algorithms, such as an autoencoder (Lusch et al. [2018]).

As we demonstrate in Fig. 3, our method could be used to quantitatively compare various hypotheses about a particular biological neural circuit’s dynamics (such as fixed point structure), by calculating similarities of various RNNs or bespoke models to data (Pagan et al. [2022], Schaeffer et al. [2020]). This task is computationally intensive, relying on assessing the dynamics of noise perturbations in the neural state space (Chaudhuri et al. [2019], Galgali et al. [2023]) or computing the locations of fixed points in a task-optimized RNN model that has similar spatial trajectories as the neural data (Mante et al. [2013], Chaisangmongkon et al. [2017]). Our method will be useful in the analysis of biological neural systems, where only recorded neural activity is accessible. To our knowledge, DSA is the first that can be used to quantitatively assess different dynamical hypotheses. We suggest that this method should be used in conjunction with shape analyses when assessing fits of computational models to data. In future work, we plan to apply DSA to experimental data.

As suggested by Fig. 2 and Fig. 4, DSA may be capturing similarity at the level of topology of the dynamics. This can perhaps be recognized from the methodology of DSA: the similarity transform is a homeomorphism between two linear systems. If the fitted HAVOK model is sufficiently accurate, then by Takens [1981] and Koopman [1931], it is possible that the model is topologically equivalent to the original system. Furthermore, Hart et al. [2020] proved that a sufficiently high dimensional embedding of a nonlinear dynamical system can perfectly predict the next observation with a simple linear readout. Thus, DSA could be thought of as quantifying how far from homeomorphic two dynamical systems are. In future work, we hope to prove this rigorously.

DSA could potentially be used for rapid alignment of Brain-Computer Interfaces (BCI) across days in a subject, a common problem due to non-stationary sampling of neurons from intracortical electrode shift, neuron death, and other noise in longitudinal BCI trials (Biran et al. [2005], Perge et al. [2013]). In fact, two recent approaches (Willett et al. [2023], Degenhart et al. [2020]) utilized Procrustes Analysis in their decoding and alignment pipeline. As demonstrated by Figs. 2, 3, and 4, an alignment method that takes dynamics into account will be useful. Karpowicz et al. [2022] utilized LFADS to align dynamics across days, but DSA may provide equal performance with less compute and data due to the method’s simplicity.

In section 3.5 we demonstrated how the DSA metric space could be used in a hypothesis-driven fashion to compare neurophysiological data recorded across training to artificial neural networks trained with different learning rules. To do so, one would train a variety neural networks with different learning rules to solve the same task as the animal model. By applying DSA pairwise to each network and the neurophysiology data, and identifying which learning rule cluster to which the experimental data aligns best, we can reject other learning rule hypotheses. DSA has multiple advantages over previous methods: These include unsupervised feature generation, which can improve classification capabilities, and abstraction from geometry, which makes the method more generically applicable across systems of different types and initial conditions.

Limitations and Compute As discussed in the DMD literature (e.g. Brunton et al. [2017]), it can be challenging to identify the optimal hyperparameters, but it is not computationally intensive to perform a grid sweep. Furthermore, we found that the rank and delay required to achieve our results was relatively small. Our Procrustes Analysis over Vector Fields method scales at best as $O(r^2)$ with the size of the DMD matrix. These issues are mitigated with parallel processing, and the code we will release is GPU-accelerated. We ran all experiments with a single V100 GPU on a departmental cluster, which each took between an hour and a day to complete, depending on the size of the datasets.

Acknowledgments The authors are grateful to Sarthak Chandra, Raymond Wang, Aran Nayebi, Ho Kyung Sung, and other members of the Fiete lab for helpful discussions and advice.

References

- Martin Schrimpf, Jonas Kubilius, Ha Hong, Najib J. Majaj, Rishi Rajalingham, Elias B. Issa, Kohitij Kar, Pouya Bashivan, Jonathan Prescott-Roy, Franziska Geiger, Kailyn Schmidt, Daniel L. K. Yamins, and James J. DiCarlo. Brain-score: Which artificial neural network for object recognition is most brain-like? *bioRxiv*, 2020. URL <https://www.biorxiv.org/content/early/2020/01/02/407007>.
- Rishidev Chaudhuri, Berk Gerçek, Biraj Pandey, Adrien Peyrache, and Ila Fiete. The intrinsic attractor manifold and population dynamics of a canonical cognitive circuit across waking and sleep. *Nature Neuroscience*, 22(9):1512–1520, 2019.
- Alan D. Degenhart, William E. Bishop, Emily R. Oby, Elizabeth C. Tyler-Kabara, Steven M. Chase, Aaron P. Batista, and Byron M. Yu. Stabilization of a brain–computer interface via the alignment of low-dimensional spaces of neural activity. *Nature Biomedical Engineering*, pages 672–685, 2020.
- Marino Pagan, Vincent D Tang, Mikio C. Aoi, Jonathan W. Pillow, Valerio Mante, David Sussillo, and Carlos D. Brody. A new theoretical framework jointly explains behavioral and neural variability across subjects performing flexible decision-making. *bioRxiv*, 2022. URL <https://www.biorxiv.org/content/early/2022/11/28/2022.11.28.518207>.

- Nikolaus Kriegeskorte, Marieke Mur, and Peter Bandettini. Representational similarity analysis - connecting the branches of systems neuroscience. *Frontiers in Systems Neuroscience*, 2, 2008.
- Maithra Raghu, Justin Gilmer, Jason Yosinski, and Jascha Sohl-Dickstein. Svcca: Singular vector canonical correlation analysis for deep learning dynamics and interpretability. *Advances in neural information processing systems*, 30, 2017.
- Alex H Williams, Erin Kunz, Simon Kornblith, and Scott Linderman. Generalized shape metrics on neural representations. In *Advances in Neural Information Processing Systems*, volume 34, pages 4738–4750, 2021.
- Lyndon R Duong, Jingyang Zhou, Josue Nassar, Jules Berman, Jeroen Olieslagers, and Alex H Williams. Representational dissimilarity metric spaces for stochastic neural networks. *arXiv preprint arXiv:2211.11665*, 2022.
- J J Hopfield. Neurons with graded response have collective computational properties like those of two-state neurons. *Proc. Natl. Acad. Sci. U. S. A.*, 81(10):3088–3092, 1984.
- J J Hopfield and D W Tank. Computing with neural circuits: a model. *Science*, 233(4764):625–633, 1986.
- K Zhang. Representation of spatial orientation by the intrinsic dynamics of the head-direction cell ensemble: a theory. *J. Neurosci.*, 15:2112–2126, 1996.
- Gianluigi Mongillo, Omri Barak, and Misha Tsodyks. Synaptic theory of working memory. *Science*, pages 1543–1546, 2008.
- Yoram Burak and Ila R Fiete. Accurate path integration in continuous attractor network models of grid cells. *PLoS Comput. Biol.*, 5(2):e1000291, February 2009.
- Anne K Churchland, Roozbeh Kiani, and Michael N Shadlen. Decision-making with multiple alternatives. *Nat. Neurosci.*, 11(6):693–702, 2008.
- David Sussillo and L F Abbott. Generating coherent patterns of activity from chaotic neural networks. *Neuron*, 63(4):544–557, 2009.
- Mark M Churchland, John P Cunningham, Matthew T Kaufman, Justin D Foster, Paul Nuyujukian, Stephen I Ryu, and Krishna V Shenoy. Neural population dynamics during reaching. *Nature*, 487(7405):51–56, 2012.
- Mikhail Khona and Ila R. Fiete. Attractor and integrator networks in the brain. *Nature Reviews Neuroscience*, 23(12):744–766, 2022.
- Saurabh Vyas, Matthew D Golub, David Sussillo, and Krishna V Shenoy. Computation through neural population dynamics. *Annual Review of Neuroscience*, 43:249–275, 2020.
- Niru Maheswaranathan, Alex Williams, Matthew Golub, Surya Ganguli, and David Sussillo. Universality and individuality in neural dynamics across large populations of recurrent networks. In *Advances in Neural Information Processing Systems*, volume 32, 2019.
- Aniruddh R. Galgali, Maneesh Sahani, and Valerio Mante. Residual dynamics resolves recurrent contributions to neural computation. *Nature Neuroscience*, 2023.
- Bernard O Koopman. Hamiltonian systems and transformation in hilbert space. *Proceedings of the National Academy of Sciences*, 17(5):315–318, 1931.
- Igor Mezić. Spectral properties of dynamical systems, model reduction and decompositions. *Nonlinear Dynamics*, 41:309–325, 2005.
- Gregory Snyder and Zhuoyuan Song. Koopman operator theory for nonlinear dynamic modeling using dynamic mode decomposition. *arXiv preprint arXiv:2110.08442*, 2021.
- Steven L. Brunton, Marko Budišić, Eurika Kaiser, and J. Nathan Kutz. Modern Koopman Theory for Dynamical Systems, 2021. URL <http://arxiv.org/abs/2102.12086>.

- David Sussillo and Omri Barak. Opening the Black Box: Low-Dimensional Dynamics in High-Dimensional Recurrent Neural Networks. *Neural Computation*, 25(3):626–649, 2013.
- Scott W. Linderman, Andrew C. Miller, Ryan P. Adams, David M. Blei, Liam Paninski, and Matthew J. Johnson. Recurrent switching linear dynamical systems, 2016. URL <http://arxiv.org/abs/1610.08466>.
- Peter J. Schmid. Dynamic mode decomposition of numerical and experimental data. *Journal of Fluid Mechanics*, 656:5–28, 2010.
- Bingni W. Brunton, Lise A. Johnson, Jeffrey G. Ojemann, and J. Nathan Kutz. Extracting spatial–temporal coherent patterns in large-scale neural recordings using dynamic mode decomposition. *Journal of Neuroscience Methods*, pages 1–15, 2016a.
- Steven L. Brunton, Bingni W. Brunton, Joshua L. Proctor, Eurika Kaiser, and J. Nathan Kutz. Chaos as an Intermittently Forced Linear System. *Nature Communications*, 8(1):19, 2017.
- Pierre Dubois, Thomas Gomez, Laurent Planckaert, and Laurent Perret. Data-driven predictions of the Lorenz system. *Physica D: Nonlinear Phenomena*, 408:132495, 2020.
- Steven L Brunton, Bingni W Brunton, Joshua L Proctor, and J Nathan Kutz. Koopman invariant subspaces and finite linear representations of nonlinear dynamical systems for control. *PloS one*, 11(2):e0150171, 2016b.
- Mason Kamb, Eurika Kaiser, Steven L. Brunton, and J. Nathan Kutz. Time-Delay Observables for Koopman: Theory and Applications. *SIAM Journal on Applied Dynamical Systems*, 19(2): 886–917, 2020.
- Floris Takens. Detecting strange attractors in turbulence. In *Dynamical Systems and Turbulence*. Warwick, 1981.
- Nicolas D. Jimenez, Bijan Afsari, and Rene Vidal. Fast Jacobi-type algorithm for computing distances between linear dynamical systems. In *2013 European Control Conference (ECC)*, pages 3682–3687, Zurich, 2013. IEEE.
- Diederik P Kingma and Jimmy Ba. Adam: A method for stochastic optimization. *arXiv preprint arXiv:1412.6980*, 2014.
- W. E. Skaggs, J. J. Knierim, H. S. Kudrimoti, and B. L. McNaughton. A model of the neural basis of the rat’s sense of direction. *Advances in Neural Information Processing Systems*, 7:173–180, 1995.
- Raymond Wang and Louis Kang. Multiple bumps can enhance robustness to noise in continuous attractor networks. *PLOS Computational Biology*, 18(10):1–38, 10 2022.
- Nikolaus Kriegeskorte and Xue-Xin Wei. Neural tuning and representational geometry. *Nature Reviews Neuroscience*, 22(11):703–718, 2021.
- Aran Nayebi, Sanjana Srivastava, Surya Ganguli, and Daniel L Yamins. Identifying Learning Rules From Neural Network Observables. In *Advances in Neural Information Processing Systems*, volume 33, pages 2639–2650, 2020.
- Blake Bordelon and Cengiz Pehlevan. The Influence of Learning Rule on Representation Dynamics in Wide Neural Networks, 2022. URL <http://arxiv.org/abs/2210.02157>.
- Ilya Sutskever, James Martens, George Dahl, and Geoffrey Hinton. On the importance of initialization and momentum in deep learning. In *Proceedings of the 30th International Conference on Machine Learning*, pages 1139–1147. PMLR, 2013.
- Daniel Kunin, Aran Nayebi, Javier Sagastuy-Brena, Surya Ganguli, Jonathan Bloom, and Daniel Yamins. Two routes to scalable credit assignment without weight symmetry. In *International Conference on Machine Learning*, pages 5511–5521. PMLR, 2020.
- Timothy P. Lillicrap, Daniel Cownden, Douglas B. Tweed, and Colin J. Akerman. Random synaptic feedback weights support error backpropagation for deep learning. *Nature Communications*, 7(1): 13276, 2016.

- Akhilan Boopathy and Ila Fiete. How to Train Your Wide Neural Network Without Backprop: An Input-Weight Alignment Perspective. In *Proceedings of the 39th International Conference on Machine Learning*, pages 2178–2205. PMLR, 2022.
- Donald O. Hebb. *The organization of behavior: A neuropsychological theory*. Wiley, New York, 1949.
- J. B. Kruskal. Multidimensional scaling by optimizing goodness of fit to a nonmetric hypothesis. *Psychometrika*, 29(1):1–27, 1964.
- Geoffrey Hinton. The forward-forward algorithm: Some preliminary investigations. *arXiv preprint arXiv:2212.13345*, 2022.
- Patrick T. Sadtler, Kristin M. Quick, Matthew D. Golub, Steven M. Chase, Stephen I. Ryu, Elizabeth C. Tyler-Kabara, Byron M. Yu, and Aaron P. Batista. Neural constraints on learning. *Nature*, 512(7515):423–426, 2014.
- Peter C. Humphreys, Kayvon Daie, Karel Svoboda, Matthew Botvinick, and Timothy P. Lillicrap. Bci learning phenomena can be explained by gradient-based optimization. *bioRxiv*, 2022. URL <https://www.biorxiv.org/content/early/2022/12/08/2022.12.08.519453>.
- Alexandre Payeur, Amy L. Orsborn, and Guillaume Lajoie. Neural manifolds and gradient-based adaptation in neural-interface tasks. *bioRxiv*, 2023. URL <https://www.biorxiv.org/content/early/2023/03/12/2023.03.11.532146>.
- Bethany Lusch, J. Nathan Kutz, and Steven L. Brunton. Deep learning for universal linear embeddings of nonlinear dynamics. *Nature Communications*, 9(1), 2018.
- Rylan Schaeffer, Mikail Khona, Leenoy Meshulam, Brain Laboratory International, and Ila Fiete. Reverse-engineering recurrent neural network solutions to a hierarchical inference task for mice. In *Advances in Neural Information Processing Systems*, volume 33, pages 4584–4596, 2020.
- Valerio Mante, David Sussillo, Krishna V. Shenoy, and William T. Newsome. Context-dependent computation by recurrent dynamics in prefrontal cortex. *Nature*, 503(7474):78–84, 2013.
- Warasinee Chaisangmongkon, Sruthi K. Swaminathan, David J. Freedman, and Xiao-Jing Wang. Computing by robust transience: How the fronto-parietal network performs sequential, category-based decisions. *Neuron*, 93(6):1504–1517, 2017.
- Allen Hart, James Hook, and Jonathan Dawes. Embedding and approximation theorems for echo state networks. *Neural Networks*, 128:234–247, 2020.
- Roy Biran, David C. Martin, and Patrick A. Tresco. Neuronal cell loss accompanies the brain tissue response to chronically implanted silicon microelectrode arrays. *Experimental Neurology*, 195(1): 115–126, 2005.
- János A. Perge, Mark L. Homer, Wasim Q. Malik, Sydney Cash, Emad Eskandar, Gerhard Friehs, John P. Donoghue, and Leigh R. Hochberg. Intra-day signal instabilities affect decoding performance in an intracortical neural interface system. *Journal of Neural Engineering*, 10(3), 2013.
- Francis R. Willett, Erin M. Kunz, Chaofei Fan, Donald T. Avansino, Guy H. Wilson, Eun Young Choi, Foram Kamdar, Leigh R. Hochberg, Shaul Druckmann, Krishna V. Shenoy, and Jaimie M. Henderson. A high-performance speech neuroprosthesis. preprint, Neuroscience, 2023. URL <http://biorxiv.org/lookup/doi/10.1101/2023.01.21.524489>.
- Brianna M. Karpowicz, Yahia H. Ali, Lahiru N. Wimalasena, Andrew R. Sedler, Mohammad Reza Keshtkaran, Kevin Bodkin, Xuan Ma, Lee E. Miller, and Chethan Pandarinath. Stabilizing brain-computer interfaces through alignment of latent dynamics. *bioRxiv*, 2022. URL <https://www.biorxiv.org/content/early/2022/11/08/2022.04.06.487388>.

Supplementary Information

5 Dynamical Similarity

We consider the problem of determining when two linear autonomous dynamical systems on \mathbb{R}^n

$$\dot{\mathbf{x}} = \mathbf{A}\mathbf{x} \quad \text{and} \quad \dot{\mathbf{y}} = \mathbf{B}\mathbf{y} \quad (7)$$

may be regarded as equivalent. One natural definition is that for all time t , there exists a linear relationship between \mathbf{x} and \mathbf{y}

$$\mathbf{y} = \mathbf{C}\mathbf{x} \quad (8)$$

Differentiating both sides with respect to time and substituting in the dynamics relationship yields an equivalent condition in terms of the system matrices \mathbf{A} and \mathbf{B}

$$\mathbf{y} = \mathbf{C}\mathbf{x} \iff \mathbf{B} = \mathbf{C}\mathbf{A}\mathbf{C}^{-1} \quad (9)$$

Thus a natural measure of *similarity* between two linear dynamical systems is

$$d(\mathbf{x}, \mathbf{y}) \equiv \min_{\mathbf{C}} \|\mathbf{B} - \mathbf{C}\mathbf{A}\mathbf{C}^{-1}\| \quad (10)$$

5.1 Computing Procrustes Alignment over Vector Fields

Unfortunately, this measure of similarity requires solving a nonconvex optimization problem. To simplify, we restrict \mathbf{C} to be orthogonal, i.e., $\mathbf{C}^{-1} = \mathbf{C}^T$ or $\mathbf{C} \in O(n)$, the orthogonal group. The problem is still nonconvex, but we can take advantage of a convenient parameterization of orthogonal matrices in terms of the *Cayley Transform*. Namely, for an arbitrary skew-symmetric matrix \mathbf{S} , the matrix

$$\mathbf{C} = (\mathbf{I} - \mathbf{S})(\mathbf{I} + \mathbf{S})^{-1} \quad (11)$$

is orthogonal and may readily be computed in deep learning libraries such as PyTorch (e.g., `C = torch.linalg.solve(I + S, I - S)`). Using this parametrization, we compute the metric with gradient descent over \mathbf{S} via the Adam optimizer.

6 Proof that the minimum similarity transform is a metric

Let A and B each be matrices in $\mathcal{R}^{n \times n}$. We wish to show that

$$d(A, B) = \min_{C \in O(n)} \|A - CBC^{-1}\|_F \quad (12)$$

is a proper metric—that is, the following three properties hold:

- Zero: $d(A, B) = 0 \iff A = B$
- Symmetry: $d(A, B) = d(B, A)$
- Triangle Inequality: $d(A, C) \leq d(A, B) + d(B, C)$

According to Williams et al. [2021], only two things are needed. First, we must show that

$$g(A, B) = \|A - B\|_F \quad (13)$$

is a metric, which is trivially true. Then we must show that the similarity transform is an isometry:

$$g(T(A), T(B)) = g(A, B) \quad (14)$$

where $T(A)$ is a map that in our case is the similarity transform.

$$g(T(A), T(B)) = \|CAC^{-1} - CBC^{-1}\|_F = \|C(A - B)C^{-1}\|_F \quad (15)$$

Using the identity that the Frobenius norm of a matrix is equivalent to the trace of the inner product with itself,

$$g(T(A), T(B)) = \text{Tr}([C(A - B)C^{-1}]^T [C(A - B)C^{-1}]) \quad (16)$$

$$= \text{Tr}(C(A - B)^T C^{-1} C(A - B) C^{-1}) \quad (17)$$

$$= \text{Tr}(C(A - B)^T (A - B) C^{-1}) = \text{Tr}(C^{-1} C(A - B)^T (A - B)) \quad (18)$$

$$= \text{Tr}((A - B)^T (A - B)) = \|A - B\|_F = g(A, B) \quad (19)$$

With the last steps using the cyclic property of the trace (Tr) and the fact that C is an orthonormal matrix.

7 Proof that the minimizer of the euclidean distance also minimizes angular distance

Let C^* be the minimizer of $\|A - CBC^{-1}\|_F$. Then we can rewrite this as above, using the trace identity:

$$\|A - CBC^{-1}\| = \text{Tr}((A - CBC^{-1})^T (A - CBC^{-1})) \quad (20)$$

which can be expanded into:

$$= \text{Tr}(A^T A) - 2\text{Tr}(A^T CBC^{-1}) + \text{Tr}(B^T B)$$

$$= \text{Tr}(A^T A) - 2 \langle A, CBC^{-1} \rangle + \text{Tr}(B^T B)$$

By minimizing the Frobenius norm, C^* must maximize the inner product $\langle A, CBC^{-1} \rangle$. The angular distance is defined as

$$\arccos \frac{\langle A, CBC^{-1} \rangle}{\|A\| \|B\|} \quad (21)$$

Due to the arccos function being monotonically decreasing, maximizing the matrix inner product therefore minimizes the angular distance.

8 Vector Fields Under Orthogonal Transformation

Here we demonstrate how Vector Fields transform. Given some linear system $\dot{x} = Ax$, the matrix A contains all the information about the vector field (Fig. 8a). Applying a single orthogonal matrix C to the left (or right) of A to yield the system $\dot{x} = CAx$ produces the plot in Fig. 8b. This is clearly a different dynamical system, as all the vectors now point away from the line attractor attractor, thereby making the system unstable instead of stable. However, applying the similarity transform CAC^{-1} preserves the dynamical structure of the linear system by rotating both the vectors and their positions on the field.

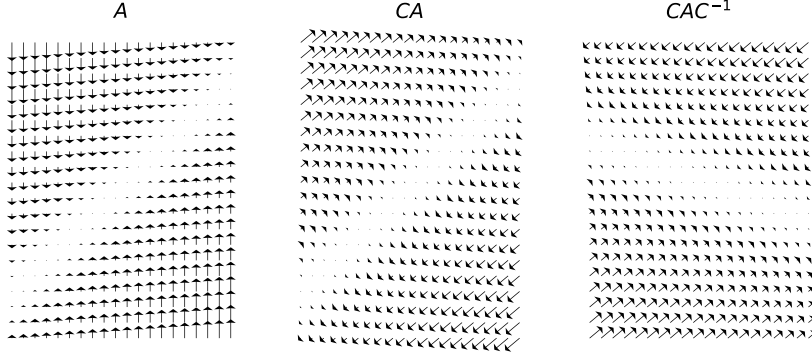


Figure 6: Vector Fields for a linear system A and two transformations. Here, C is an orthogonal matrix. The size of the arrow represents the magnitude of the vector, so the small dots are zeros, indicating the line attractor.

9 DSA pseudocode

Algorithm 1 Dynamic Similarity Analysis

Input: $X_1, X_2 \in \mathbb{R}^{n \times t \times d}$, p, r

Output: Similarity transform distance d between the two dynamics matrices

procedure DELAYEMBEDDING(X, p)

Initialize $H \in \mathbb{R}^{n \times (t-p) \times p \times d}$

$H = \begin{bmatrix} X[:, 1 : p, :] \\ X[:, 2 : p + 1, :] \\ \dots \\ X[:, t - p + 1 : t, :] \end{bmatrix}$ reshaped to $\mathbb{R}^{n \times (t-p) \times p \times d}$

return H

end procedure

procedure DMD(H, r)

Initialize $A \in \mathbb{R}^{r \times r}$

$H' = H[:, 1 : r]$

$H = H[:, r + 1 : t]$

Decompose $H = U\Sigma V^T$, and $H' = U'\Sigma'V'^T$

Reduce Rank: $V = V[:, : r]$, and $V' = V'[:, : r]$

Compute A such that $V' = AV$ (OLS or Ridge Regression, depending on regularization)

return A

end procedure

$H_1 = \text{DELAYEMBEDDING}(X_1, p)$

$H_2 = \text{DELAYEMBEDDING}(X_2, p)$

$A_1 = \text{DMD}(H_1, r)$

$A_2 = \text{DMD}(H_2, r)$

$d = \min_{C \in O(r)} \|A_1 - CA_2C^{-1}\|$

10 FlipFlop task MDS clustering by activation

Here, we plotted the same MDS scatterplots as in Fig. 2 in the main text. The only difference here is that the networks are colored by activation function instead of architecture. Evidently, the same conclusion holds here as in Fig. 2.

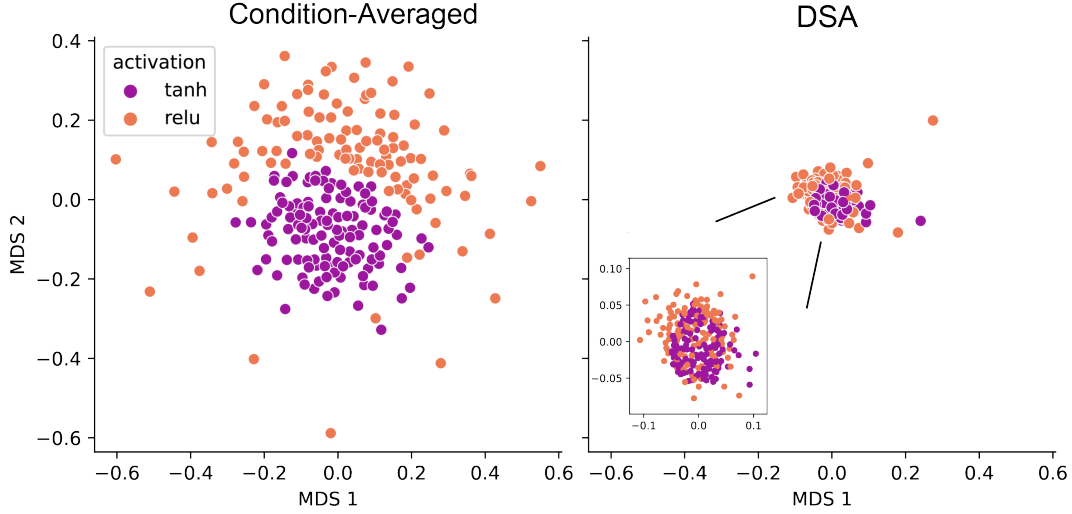


Figure 7: **Same dynamics, different shape, only identified as similar with DSA.** Dots indicate a single trained network. Analysis of RNNs trained on the 3-bit flipflop task. **b.** MDS Projection of the Dissimilarity Matrix computed across condition-averaged hidden states between each RNN (activation function indicated by color). In this view of the data, RNNs cluster by activation function. **c.** MDS Embedding of the dissimilarity matrix generated from DSA of the same set of RNNs as in **b.** Here, RNNs do not cluster by activation function.

11 Flip-Flop task HAVOK grid sweep

We fit HAVOK models with a range of ranks and delays, and assessed their fits in three different ways: R^2 , MSE, and Pearson correlation between the predicted state from HAVOK and the true data, across 10 different models. Note that we did not exhaustively test all trained models and a large range of ranks and delays for the sake of efficiency. Here we see that across all metrics, steadily increasing rank and number of delays (listed as lag) improves the performance of the model. Across all metrics, there appears to be a Pareto Frontier which implies that the specific choice of rank and lag is not important. Furthermore, the metrics appear to saturate relatively quickly.

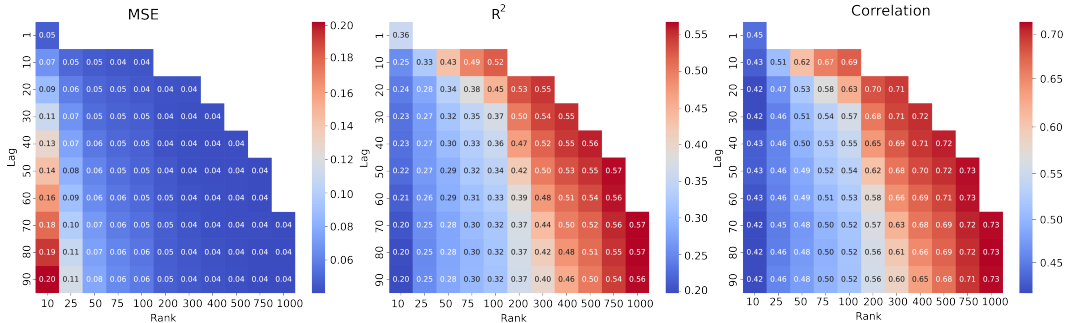


Figure 8: Mean HAVOK fits for three different scores across a variety of delays and ranks. The unfilled elements occurs when the rank is larger than the number of lags times the delays. Each model was computed over 15 Principal Components of the data, which had 128 trials with 500 timesteps each.

12 Condition-Averaged Aligned Dynamics Systems Equations

Here we describe the process we used to sample from the three dynamical systems with different attractors, and adversarially optimize input so that the condition averages are indistinguishable. This describes the systems tested in Figure 3 in the main text.

Bistable System

$$\dot{x}_1 = ax_1^3 + bx_1 + u + \epsilon_2 \quad (22)$$

$$\dot{x}_2 = cx_2 + u + \epsilon_2 \quad (23)$$

We randomly sample parameters for the system once from: $a \sim U(-5, -3)$ $b \sim U(4, 7)$ $c \sim U(-4, -2)$ and noise at each time step sampled i.i.d. $\epsilon \sim N(0, 0.05)$ We update the system with an Euler update with $dt = 0.01$. u is defined as a constant in $\{-0.1, 0.1\}$ to drive the system to either of the stable fixed points.

Line Attractor We define the eigenvectors and eigenvalues to get the linear system:

$$\Lambda = \begin{pmatrix} -1 & 0 \\ 0 & 0 \end{pmatrix} \quad V = \begin{pmatrix} 1 & 1 \\ 1 & 0 \end{pmatrix} \quad A = V\Lambda V^{-1} \quad (24)$$

$$\dot{x} = Ax + \hat{u} \quad (25)$$

Point Attractor

$$A = \begin{pmatrix} -0.5 & 0 \\ 0 & -1 \end{pmatrix} \quad (26)$$

$$\dot{x} = Ax + \hat{u} \quad (27)$$

Adversarial optimization scheme to align condition averages We apply a simple feedback linearization scheme to control the condition averages of the line and point attractor. We simulate batches of trajectories simultaneously in order to calculate condition averages for the optimization scheme. First, we identify the condition averages \bar{y} from the bistable system, which are previously calculated. At each step of the latter two systems, we calculate the condition averages \bar{x} . Then we define \hat{u} , the input that aligns the condition averages between systems:

$$\hat{u} = -A\bar{x}_t + \frac{1}{\alpha}(\bar{y}_{t+1} - \bar{x}_t) \quad (28)$$

Thus, when we apply the Euler update with time step α , our system is defined by

$$x_{t+1} = x_t + \alpha(Ax_t - A\bar{x}_t) + \bar{y}_{t+1} - \bar{x}_t \quad (29)$$

Which makes our condition-averaged dynamics of the line and point attractor system

$$\bar{x}_{t+1} = \bar{y}_{t+1} \quad (30)$$

13 Ring Attractor Dynamics

We implemented the ring attractor defined in Wang and Kang [2022], defined by the following equation:

$$\tau \frac{dg}{dt} = -g + W^T \phi(g) + A \pm \gamma b(t) + \xi(x, t) \quad (31)$$

Here, g describes the synaptic activation along the ring, and ϕ is the neural transfer function that converts these into firing rates. In our deformation analysis we only changed ϕ after simulation, which does not affect the ring topology but modifies geometry. To stabilize the dynamics of the ring for path integration, there are in fact two rings, each with their connectivity profile slightly offset, and with the \pm term separately $+$ for one ring and $-$ for the other. A describes the resting baseline input to the neurons, whereas b describes the driving input that the network seeks to integrate, and γ is a coupling term. τ describes the time constant, and ξ describes the activity noise term. W of course describes the weight matrix that has local excitatory connectivity and global inhibitory connectivity between neurons in the ring.

14 Ring Attractor Deformation

Here we present two other visualizations that demonstrate how the ring transforms under the β parameter in the sigmoid function as well as the scaling parameter. In Fig. 9 a and b we display the activation along the neurons in the ring for different scale values of the parameters (lighter indicates larger, following the same colorbar in the main text Fig. 4). Under scaling of β (a), the bump becomes much tighter in width, leading to further sparsity of the activation. In a state-space view, a tighter bump means that the neural activity hugs the axes of the neural space, which implies that the bump becomes progressively less planar. This is then demonstrated in Fig. 9b, in which we computed the explained variance ratio (EVR) of the first two PCs across the β parameters we tested. At first, the first two PCs summarize close to 100% of the variance, but at large β s, this drops to only around 40%. On the other hand, the ring remains planar under global scaling by this same analysis (Fig. 9d).

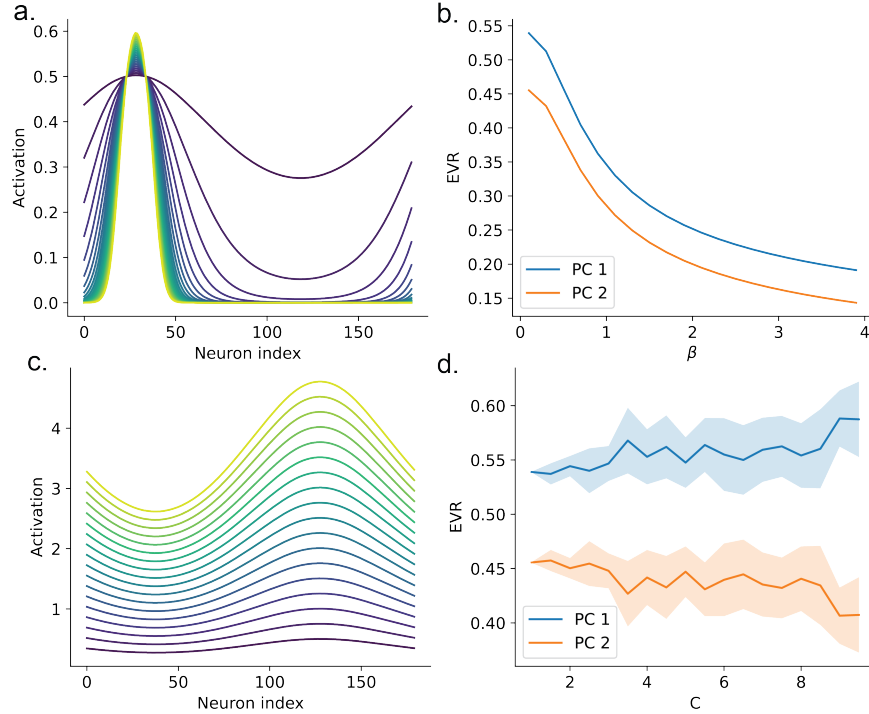


Figure 9: Deformation of the ring under bending (a,b) and scaling (c,d). **a,c.** Neural activity of the network at a snapshot in time during simulation. Different colors represent different value of the scaling parameter—brighter indicates larger. **b,d.** Visualization of the PCs across these transformations demonstrates that increasing β makes the ring progressively less scalar, whereas scaling does not.

15 Line Attractor Deformation

We use the same line attractor matrix as in section 12:

$$\Lambda = \begin{pmatrix} -1 & 0 \\ 0 & 0 \end{pmatrix} \quad V = \begin{pmatrix} 1 & 1 \\ 1 & 0 \end{pmatrix} \quad A = V\Lambda V^{-1} \quad (32)$$

However, the dynamics are slightly different, as we introduce a nonlinear activation function:

$$\dot{x} = A \tanh(\beta x) + u + \epsilon \quad (33)$$

Where $u = \{1, -1\}$ and is constant across both dimensions to drive the system along the attractor in different directions. Here, β is a scalar that affects the curvature of the attractor, as demonstrated by the vector fields of this system at three example values (Fig. 10a). We applied the same analysis as in Fig.4 in the main text and found the exact same results—Procrustes distance increases in magnitude as

the two β values being compared increases, but DSA is invariant. This adds to the evidence that DSA captures the topology of a dynamical system.

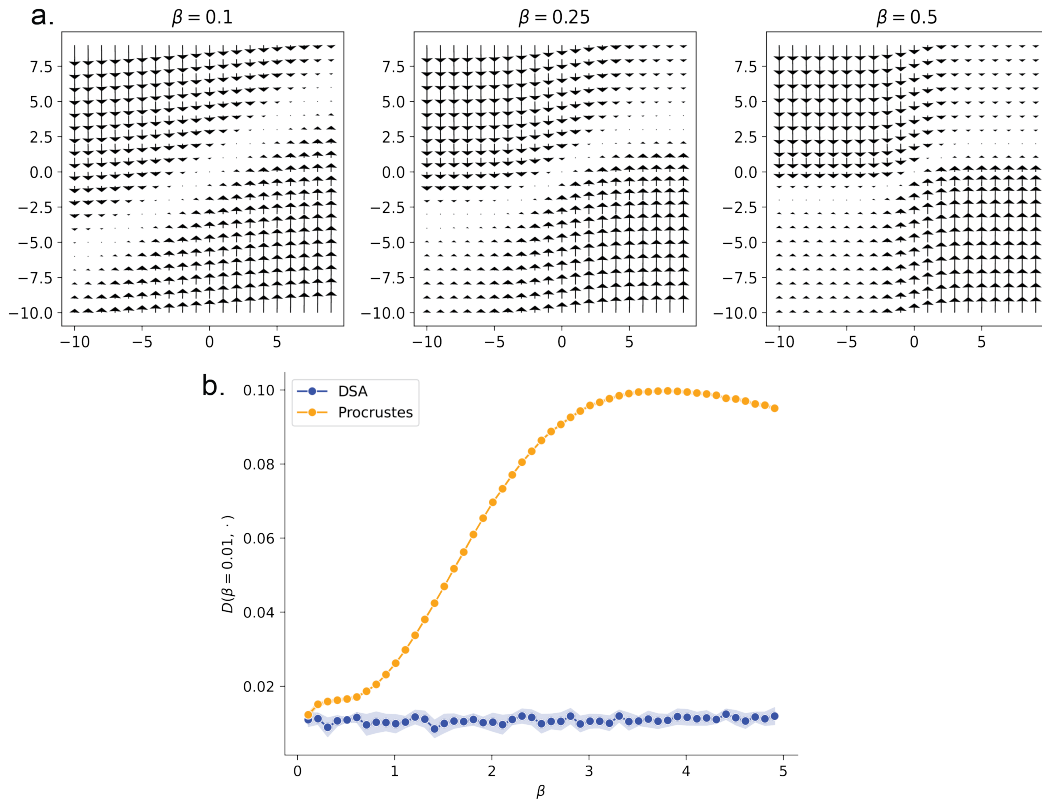


Figure 10: **DSA is invariant under geometric deformations when applied to a line attractor.** **a.** Demonstration of how the vector field transforms under β . Here, the line attractor becomes more s-shaped at higher β values. **b.** Procrustes and DSA similarity to the smallest tested β (0.1) at various values. Shaded region indicates standard error of the mean over 10 simulations.